

Integrated Conjugated Microporous Polymers/Carbon Nanotube Composite Boosting Superior Anodic Lithium Storage Behavior

Jie Yu,^[a, b] Suriguga Li,^[a] Zhenjun Si,^{*[a]} Bo Gao,^[a] Xiaoling Lv,^[a] and Heng-guo Wang^{*[b]}

Conjugated microporous polymers (CMPs) with redox-active sites have attracted extensive notice in rechargeable lithium-ion batteries (LIBs) due to their extended π -conjugated structure, uniform porosity, and low solubility. However, poor electrical conductivity and low utilization of active sites limit their application in large-scale energy storage systems (ESS). Herein, we synthesized two carbonyl-rich imine-based CMPs by the polycondensation reaction between tetromino-benzoquinone and aldehydes, and integrated them with carbon nanotubes

(TB-CMP@CNT and TBP-CMP@CNT). The composites display good electrochemical performances as anode-active materials of LIBs, which benefits from abundant redox-active units, stable π -conjugated framework, and fast Li^+ diffusion kinetics. Especially, TBP-CMP@CNT has a high reversible capacity of 954.6 mAh g^{-1} at 50 mA g^{-1} , a long cycle stability at 1 A g^{-1} with no decrease in capacity after 1000 cycles, and superior rate performance of 221.5 mAh g^{-1} at 2 A g^{-1} .

Introduction

The widespread use of portable electronics, electric vehicles, and significant energy storage stations relies on the development of rechargeable batteries, especially lithium-ion batteries (LIBs).^[1–5] However, the inorganic electrode materials used for commercial LIBs have gradually shown concern about recycle, rising price, raw materials and energy consumption for mining. In this context, to meet the increasingly stringent environmental requirements and reduce carbon footprint, organic materials have emerged as ideal candidates for electrode materials of next-generation sustainable LIBs due to their availability from accessible natural sources and biomass, non-reliance on rare materials, and easy recycle and degradation.^[6–12] Especially, the variable structure of organic materials endows them with designable and controllable electrochemical properties.^[13–17] However, there are some problems for organic materials that need to be overcome. For example, the relatively low conductivity and high solubility in organic electrolyte of organic compounds will inevitably lead to their lower active site utilization and poor cycling stability.^[18–21]

Conjugated microporous polymers (CMPs) consist of periodic units linked by covalent groups, which are unique porous and amorphous polymers.^[22–25] Due to the extended π -conjugated structure, uniform porosity, and good chemical and thermal stability, they are an ideal candidate electrode material for LIBs.^[26–29] Noteworthy, their microporous structure endows them with more exposed active sites and faster ion conduction rate in the electrochemical reaction, thereby exhibiting excellent electrochemical performance.^[30,31] Especially, their structure diversity resulted from the variable periodic units and connecting patterns/reaction gives them infinite possibilities for their application in LIBs. Moreover, functional groups with electrochemical activity (such as $\text{C}=\text{O}$ and $\text{C}=\text{N}$) can be introduced into the conjugated structure as periodic units by a bottom-up strategy.^[32–35] And the “doping” of nitrogen and oxygen heteroatoms can promote the superlithiation process of aromatic rings, thus giving a surprisingly high theoretical capacity. However, the as-obtained CMPs usually show the bulk and rigid characteristics, which leads to a smaller proportion of active site exposure and limits the ionic diffusivity in the structure. To solve this problem, mechanical exfoliation of the layered organic structure has been demonstrated to be an effective strategy. In addition, growing CMP *in-situ* on carbon nanotubes (CNTs) is a “kill two birds with one stone” strategy,^[36–38] which not only generates the few-layered CMPs, but also enhances the conductivity, therefore, activating more active sites for lithium storage, improving the utilization efficiency of redox sites, and boosting superior anodic lithium storage behavior.

Herein, two carbonyl-rich imine-based conjugated microporous polymers (TB-CMP and TBP-CMP) synthesized by linking tetromino-benzoquinone (TABQ) with terephthalaldehyde (BDA) and 4,4'-biphenyldicarboxaldehyde (BPDA) were grown *in-situ* on CNTs. In this way, the existing CNTs boost the lithium storage capacity of the active sites of the introduced $\text{C}=\text{O}$ and

[a] J. Yu, S. Li, Prof. Z. Si, Dr. B. Gao, Dr. X. Lv
Materials Science and Engineering, Changchun University of Science and Technology, 7989 Weixing Road, Changchun 130022, P. R. China
E-mail: szj@cust.edu.cn

[b] J. Yu, Prof. H.-g. Wang
Key Laboratory of Polyoxometalate and Reticular Material Chemistry of Ministry of Education and Faculty of Chemistry, Northeast Normal University,
5628 Renmin Street, Changchun, 130024, P. R. China
E-mail: wanghengguo@cust.edu.cn

 Supporting information for this article is available on the WWW under <https://doi.org/10.1002/batt.202200429>

 An invited contribution to a Special Collection on Organic Batteries

the newly generated C=N as well as the superlithiation process of benzene ring. Benefiting from the synergistic effect of the thin layer of electro-active CMPs and the introduction of CNTs, TBP-CMP@CNT anode for LIBs has good electrochemical performance, including a high specific capacity of 954.6 mAh g^{-1} at 0.05 A g^{-1} , long-term cycling stability with 1000 cycles at 1 A g^{-1} without capacity degradation, and a good rate performance of 221.5 mAh g^{-1} at 2 A g^{-1} . In contrast, TBP-CMP show more superior electrochemical performance than its TB-CMP counterparts, which is attributed to the extending conjugated structure.

Results and Discussion

Figure 1 shows a schematic diagram of the synthetic routes of TB-CMP@CNT and TBP-CMP@CNT. Clearly, the carbonyl-rich imine-based CMPs were synthesized by Schiff-base reaction using TABQ and BPDA/BDA as structural units (Figure S1). The resulting CMPs contain abundant active sites (C=O and C=N) as well as polycyclic aromatic systems, which are conducive to the heteroatom-driven superlithiation process. In addition, the in-situ growth of CMP on CNTs can avoid the generation of the bulk CMP, lead to the exposure of more active sites and improve the electronic conductivity.

To confirm the structural information of CMPs and CMPs@CNT, various characterizations were carried out. Firstly, the microscopic morphology of various samples is observed by scanning electron microscope (SEM). There are some aggregated rod-like structures with different sizes (Figure S2a), proving the disorder nature of TBP-CMP. At the same time, the morphology of TBP-CMP@CNT can be seen as some particles attached to CNTs (Figure S2b), indicating the successful

composite of TBP-CMP and CNTs. Similarly, the morphology of TB-CMP is irregularly clustered (Figure S2c) and some particles attached to CNTs are observed for TB-CMP@CNT (Figure S2d). And transmission electron microscope (TEM) analysis is performed to gain further insight into the structure of the TBP-CMP@CNT (Figure 2a, b). It shows the obvious core-shell structure, indicating that TBP-CMP is successfully grown in-situ on the CNT surface. Then, Fourier transforms infrared (FT-IR) spectroscopy is performed to confirm the successful synthesis of the resulting samples. Figure 2(c) shows the FT-IR spectra of BPDA, TABQ, TBP-CMP, and TBP-CMP@CNT. In the FT-IR spectrum of TBP-CMP, a strong C=N stretching vibration peak can be observed at 1605 cm^{-1} , indicating the formation of imine bonds by the reaction between BPDA and TABQ. And a stretching vibration peak belonging to the C=O group on the benzoquinone unit is observed at 1670 cm^{-1} . In addition, small peaks near 1697 cm^{-1} and broad peaks near 3420 cm^{-1} could also be observed in the FT-IR spectrum, which is attributed to the vibrational peaks of aldehyde and amino at the marginal ends of the synthesized CMP. The FT-IR spectrum of TBP-CMP@CNT is consistent with TBP-CMP, indicating the structural consistency of TBP-CMP in TBP-CMP@CNT. The peak of TBP-CMP@CNT between 4000 and 3500 cm^{-1} could be attributed to unbound/free hydroxyl groups or water molecules adsorbed by CNT, and intermolecular hydrogen bonds between the carboxyl and phenolic groups on its surface. Similar results can be obtained in the FT-IR spectrum of TB-CMP/TB-CMP@CNT (Figure S3). The peaks at 1670 cm^{-1} and 1600 cm^{-1} belong to the stretching vibration peaks of the C=O group and the newly generated C=N group, and there are also characteristic peaks belonging to CNTs in the FT-IR spectrum of TB-CMP@CNT between 4000 and 3500 cm^{-1} . The above results demonstrate the successful synthesis of two CMPs and the corresponding CMPs@CNT. Furthermore, XRD tests are performed on TBP-CMP and TB-CMP to verify their degree of crystallinity (Figure S4). A broad peak at 22.5° appears in the XRD patterns of TBP-CMP and TB-CMP, indicating that both CMPs have no definite lattice structure and are amorphous. Then, the properties of the carbon component in the TBP-CMP@CNT composites are investigated by Raman spectroscopy (Figure S5). There are two peaks at 1340 cm^{-1} and 1580 cm^{-1} for TBP-CMP@CNT, which can be corresponded to the D peak representing the C-atom lattice defects and the G peak representing the in-plane stretching vibration of the C-atom sp² hybridization. The intensity ratio (I_D/I_G) value is 0.743, representing a high number of structural defects in this composite. Furthermore, the porous structure of TBP-CMP@CNT is investigated using the Brunauer-Emmett-Teller (BET) method. Figure 2(d) shows the nitrogen adsorption-desorption isotherm of TBP-CMP@CNT. It can be observed that when $P/P_0 = 1$, no plateau has been formed, and the adsorption has not yet reached saturation, which is a typical type II curve. The line shape reflects unrestricted monolayer-multilayer adsorption, which is consistent with the microscopic composite structure of TBP-CMP@CNT. Moreover, the calculated BET surface area value is $308 \text{ m}^2 \text{ g}^{-1}$. And the pore size distribution of TBP-CMP@CNT (Figure 2e) shows that the pore size of the composite is mainly distributed around

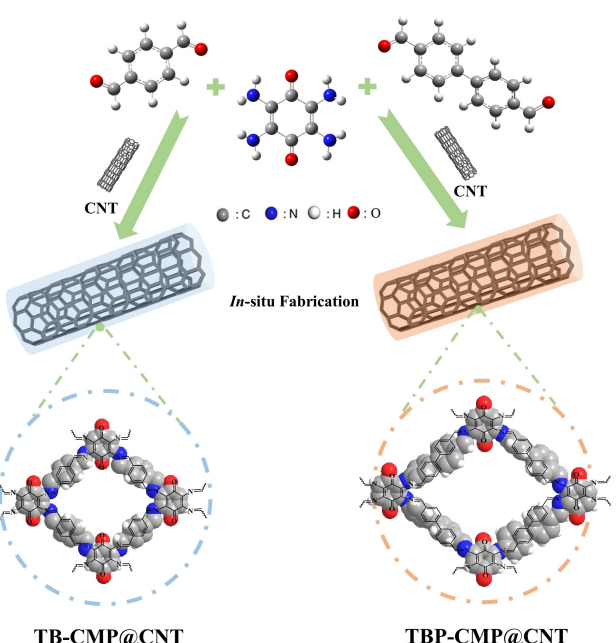


Figure 1. Synthetic routes of TB-CMP@CNT and TBP-CMP@CNT.

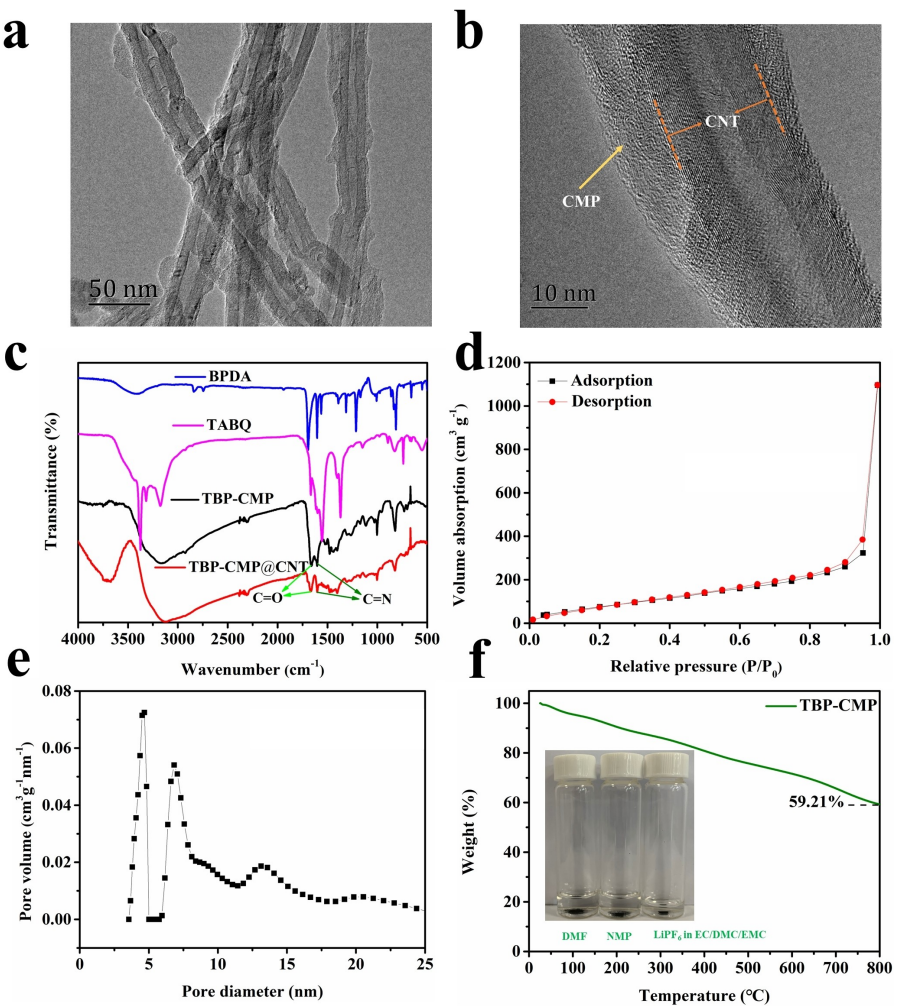


Figure 2. a) TEM and b) HRTEM images of TBP-CMP@CNT. c) FT-IR spectra of TBP-CMP@CNT, TBP-CMP, TABQ, and BPDA. d) N_2 adsorption-desorption isotherms of TBP-CMP@CNT. e) The pore-size distribution of TBP-CMP@CNT. f) TGA curve of TBP-CMP (the inset shows the chemical stability of TBP-CMP).

3 nm, indicating that the TBP-CMP@CNT composite belongs to a dense mesoporous structure. The large specific surface area and the presence of many pore sizes facilitate the adsorption of lithium ions by TBP-CMP@CNT, thus improving its electrochemical properties as an electrode material for LIBs. Finally, the stability of two CMPs is verified. The thermal stability of TBP-CMP and TB-CMP is first tested by the thermogravimetric (TG) curves in the temperature range of 25–800 °C under nitrogen. It can be seen that the weight loss ratio of both TBP-CMP and TB-CMP is less than 5% when the temperature rises from room temperature to 100 °C (Figures 2f and S6). As the subsequent temperature increases, TBP-CMP and TB-CMP slowly lost weight, representing a gradual breakdown of the structure. The weight retention is 59.21% for TBP-CMP and 59.17% for TB-CMP when the temperature was increased to 800 °C, indicating that both CMPs have excellent thermal stability. Then their solubility in different chemical reagents is also tested. Obviously, TBP-CMP and TB-CMP can be stable in DMF, NMP and electrolyte (inset of Figure 2f and Figure S6), indicating their excellent chemical stability.

Subsequently, CR2025 type coin cell was assembled with various CMPs as anode materials and lithium foil as counter electrode. And the electrochemical performance is tested in the voltage range of 0.01–3 V. Figure 3(a) shows the cyclic voltammetry (CV) curves of TBP-CMP@CNT at a scan rate of 0.1 mV s⁻¹. It can be seen that four distinct reduction peaks at 2.5, 1.5, 0.76 and 0.5 V in the first cycle, in which the reduction peaks at 2.5 and 1.5 V correspond to the binding of C=O and C=N groups to lithium ions. The reduction peaks at 0.76 and 0.5 V are related to the formation of solid electrolyte interphase (SEI) films and the lithium ions combined with the unsaturated carbon on the aromatic ring. And the oxidation peak observed at around 2.4 and 1.1 V corresponds to the detachment of lithium ions.^[40,41] In the next curve, the CV curves remain essentially same shape, indicating the reversible and electrochemical stability. And there was no obvious redox peak, consistent with the inconspicuous charge/discharge plateau in the GCD curves (Figure 3b). Similarly, the same results are observed in the CV curves for TB-CMP@CNT (Figure S7a). The irreversible reduction peak is also observed in the initial cycle resulted from the formation of stable SEI film, and the CV

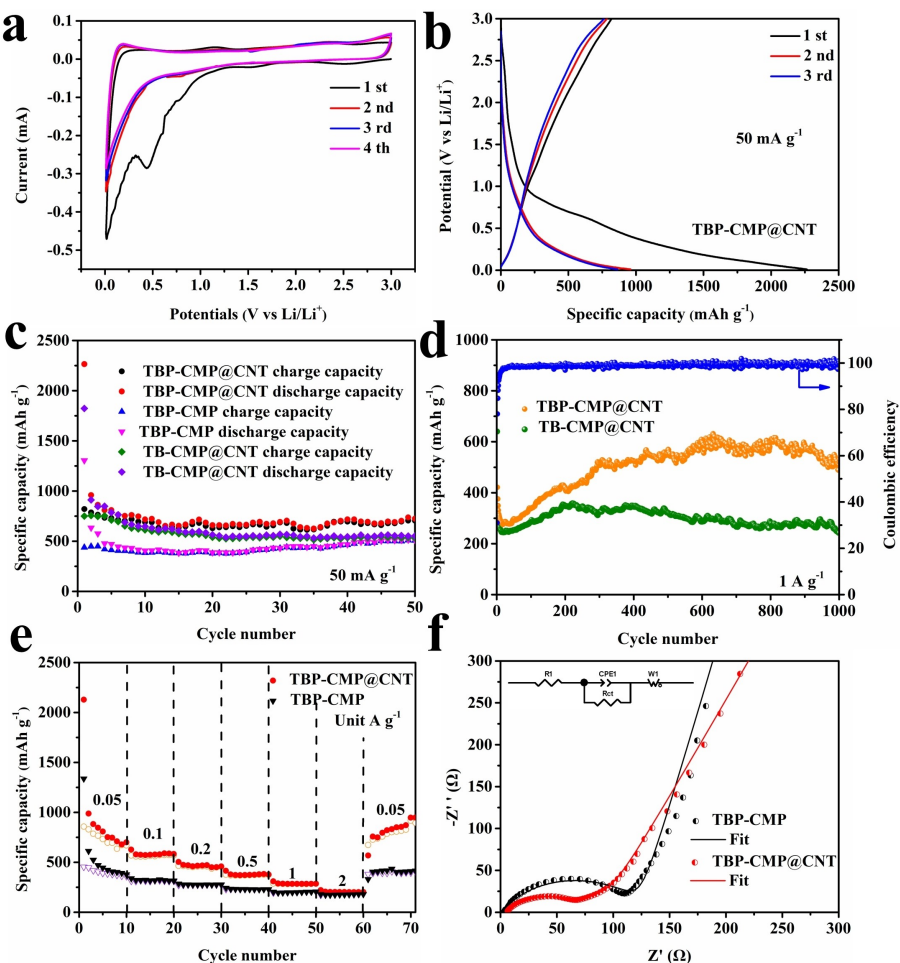


Figure 3. a) CV curves of TBP-CMP@CNT at 0.1 mVs^{-1} . b) Galvanostatic discharge/charge profiles of TBP-CMP@CNT at 0.05 A g^{-1} . c) Cycling performance of various samples at 0.05 A g^{-1} . d) Long cycling performance of TBP-CMP@CNT and TB-CMP@CNT at 1 A g^{-1} . e) Rate performance of TBP-CMP@CNT and TBP-CMP. f) Nyquist plots of pristine TBP-CMP@CNT and TBP-CMP.

curves are almost constant in the subsequent cycles, suggesting that the electrochemical reaction process is also reversible and stable. The charge and discharge capacities of TBP-CMP@CNT in the first cycle at 50 mA g^{-1} are $820/2264.5 \text{ mAh g}^{-1}$ with the Coulombic efficiency (CE) of 36.21% (Figure 3b). The low initial CE results from the formation of the SEI film as well as the decomposition of the electrolyte. Then the discharge capacities stabilize at 954.6 and 857.9 mAh g^{-1} for the 2nd and 3rd cycle, corresponding to the CEs of 81.8% and 88.6%, respectively. Similar results can be observed for the charge/discharge curves of TB-CMP@CNT at 50 mA g^{-1} , but it shows a lower specific capacity compared to TBP-CMP@CNT (Figure S7b). In addition, we also test the electrochemical performance of two pure CMPs at 50 mA g^{-1} (Figure S8). Clearly, CMPs show low capacities, which confirms the importance of the introduction of CNTs resulted from the enhanced electrical conductivity and the more exposed active sites.^[42,43] In addition, TBP-CMP shows higher specific capacity compared with its TB-CMP counterparts resulted from the large pore and extending polycyclic aromatic systems. Figure 3(c) shows the cycling performance of TBP-CMP@CNT, TB-CMP@CNT and TBP-CMP at 50 mA g^{-1} . TBP-CMP@CNT still has a

specific capacity of 737.2 mAh g^{-1} after 50 cycles, which is higher than that of TB-CMP@CNT (550.8 mAh g^{-1}) and TBP-CMP (510.6 mAh g^{-1}). Subsequently, the long-cycle stability of TBP-CMP@CNT and TB-CMP@CNT at higher current densities is also tested. As shown in Figure 3(d), both TBP-CMP@CNT and TB-CMP@CNT maintain good long-cycle stability, in contrast, TBP-CMP@CNT has higher specific capacity (521.2 mAh g^{-1}) than TB-CMP@CNT (242.8 mAh g^{-1}) after 1000 cycles at 1 A g^{-1} . The increasing capacity as the cycle proceeds is mainly due to the gradual activation of the different electro-chemically active groups in the TBP-CMP@CNT and TB-CMP@CNT.^[40,43] Stability tests have confirmed that TBP-CMP does not dissolve in the electrolyte, and the electrode materials from the disassembled cell after cycling still show insolubility (Figure S9), thus showing long-term cycling stability. Furthermore, the rate performance of CMP and CMP@CNT is tested at different current densities from 0.05 to 2 A g^{-1} . The rate capacities of TBP-CMP@CNT are $882.4, 574.3, 473.7, 378.3, 309.9, \text{ and } 221.5 \text{ mAh g}^{-1}$, respectively (Figure 3e), which is significantly higher than that of TBP-CMP. When the current density is restored to 0.05 A g^{-1} , the specific capacities of TBP-CMP@CNT recover to 854.7 mAh g^{-1} with an upward trend, indicating high structural stability at high current

density. By contrast, TB-CMP@CNT shows rate capacities of 781.7, 436.3, 361.4, 305.2, 240.4, and 192.4 mAh g⁻¹, respectively (Figure S10a). And when the current density is restored to 0.05 A g⁻¹, the specific capacity of TB-CMP@CNT is restored to 488.1 mAh g⁻¹. It can be clearly seen that the rate performance of TB-CMP@CNT is also better than that of TB-CMP. Moreover, TB-CMP@CNT shows a lower specific capacity than TBP-CMP@CNT. To analyze why TBP-CMP@CNT has more excellent lithium storage performance, the electrochemical impedance spectra (EIS) of various samples in the initial state are tested. As shown in Figure 3(f), the inset is the equivalent circuit model of Nyquist plots. Among them, R_1 represents the inner resistance, R_{ct} represents the charge-transfer resistance, CPE1 is a constant phase element, while W_1 is the Warburg impedance. And the charge transfer resistances (R_{ct} s) of TBP-CMP@CNT, and TB-CMP are 70.2 Ω, 109.3 Ω, respectively. Moreover, the R_{ct} s of TB-CMP@CNT and TB-CMP are 76.1 Ω and 154.6 Ω, respectively (Figure S10b). It is clear that the composites with CNT have smaller R_{ct} and TBP-CMP shows smaller R_{ct} than that of TB-CMP.

That is say, the presence of CNT and extending conjugation structure show minor charge transfer resistance and higher ionic conductivity during the electrochemical reaction, which can explain the better rate performance of TBP-CMP@CNT.

To analyze the differences in reaction kinetics between TBP-CMP@CNT and TB-CMP@CNT, their CV curves are recorded at different scan rates. The CV curves of TBP-CMP@CNT keep the same shape and the integrated area of the curve increases with the increasing scan rate from 0.1 to 1.0 mV s⁻¹ (Figure 4a), indicating that the capacitive effect contributes to the capacity during the charging and discharging processes. The linear fit b values for TBP-CMP@CNT are subsequently calculated according to the classic formula ($i = av^b$). When the value of b is 0.5, it proves that the electrochemical process is controlled by diffusion behavior, and when the value of b is 1.0, it proves that is controlled by capacitive behavior.^[44] As shown in Figure 4(b), the b values at the corresponding redox peaks of the TBP-CMP@CNT are all in the range of 0.5–1.0, indicating that its lithium storage mechanism is controlled by pseudocapacitive-

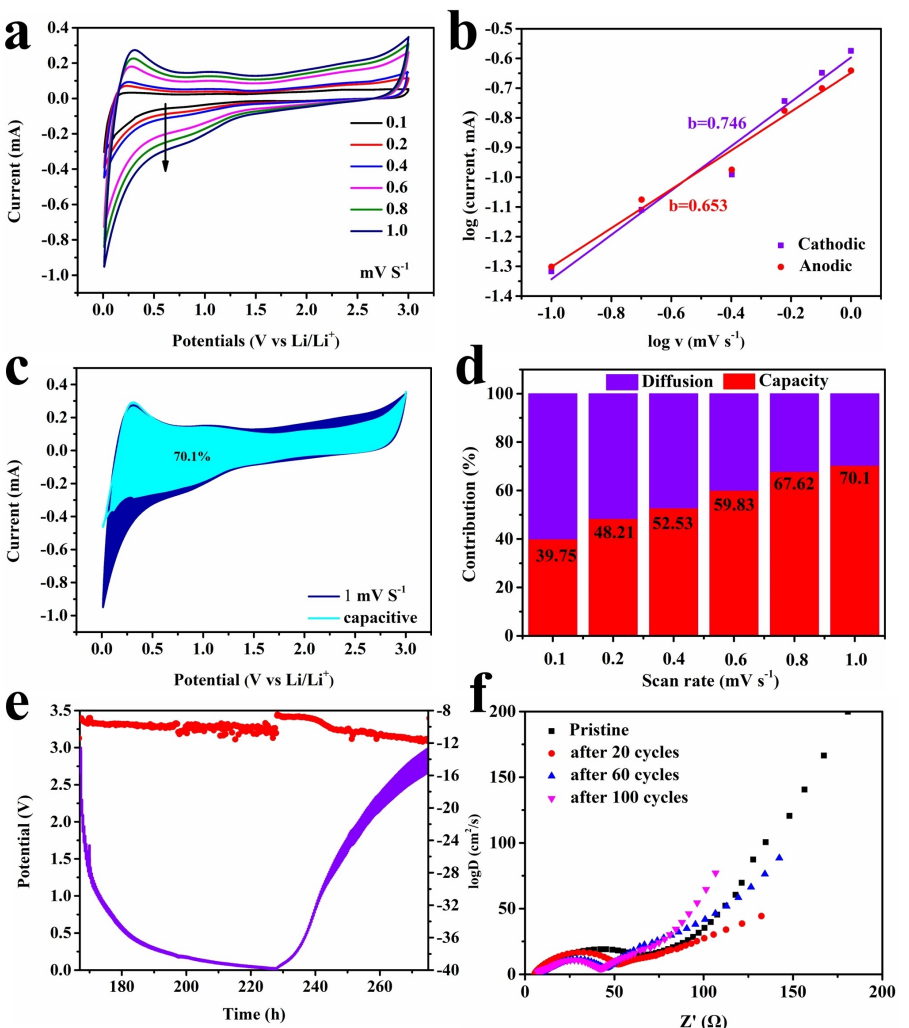


Figure 4. a) CV curves of TBP-CMP@CNT at different scan rates and b) b-value analysis using the relationship between the peak currents and scan rates. c) Separation of the capacitive and diffusion-controlled current contribution of TBP-CMP@CNT at 1 mV s⁻¹ and d) the contribution ratio of the capacitive capacities and diffusion-controlled capacities at different scan rates. e) GITT curves and corresponding Li⁺ diffusion coefficient at discharge/charge state of TBP-CMP@CNT. f) Electrochemical impedance spectra of TBP-CMP@CNT after different cycles.

diffusion hybrid control kinetics. The same result can be obtained for TB-CMP@CNT (Figure S11a, b). The contribution ratio of capacitance control and diffusion control of TBP-CMP@CNT in the electrochemical reaction process is then quantified according to the classic formula ($i(V) = k_1v + k_2v^{1/2}$).^[45] As depicted in Figure 4(c), TBP-CMP@CNT exhibits a capacitive contribution of 70.1% at 1.0 mVs^{-1} , and the capacitance contribution of TBP-CMP@CNT increased from 39.75% to 70.1% when the scan rate increased from 0.1 mVs^{-1} to 1 mVs^{-1} (Figure 4d). By contrast, TB-CMP@CNT exhibits a capacitive contribution of 61.2% at 1.0 mVs^{-1} (Figure S11c), and the capacitance contribution increased from 33.5% to 61.2% (Figure S11d). The fast lithium storage kinetics especially at high rates further explain the reason for the superior electrochemical properties of TBP-CMP@CNT compared to TB-CMP@CNT. To further analyze the reaction kinetics of TBP-CMP@CNT and TB-CMP@CNT, the galvanostatic intermittent titration technique (GITT) is performed and the corresponding ion diffusion coefficients are calculated according to formula.^[46]

$$D_{\text{Li}^+} = \frac{4}{\pi\tau} \left(\frac{m_B V_M}{M_B S} \right)^2 \left(\frac{\Delta E_s}{\Delta E_t} \right)^2$$

The same shapes of the GITT curves for TBP-CMP@CNT (Figure 4e) and TB-CMP@CNT (Figure S11e) indicate that the electrochemical reaction process in continuous charge and discharge is very close to the quasi-equilibrium state. And the diffusion coefficient of TBP-CMP@CNT ($\log D$ ranges from -8 to $-12 \text{ cm}^2 \text{s}^{-1}$) is slightly higher than that of TB-CMP@CNT ($\log D$ ranges from -10 to $-12 \text{ cm}^2 \text{s}^{-1}$). In addition, the EIS is tested before and after 20, 60 and 100 cycles for TBP-CMP@CNT (Figure 4f). Clearly, the R_{ct} value of the TBP-CMP@CNT gradually decreases from the initial 70.2Ω to 41.2Ω after 100 cycles. Similarly, the R_{ct} value of TB-CMP@CNT also decreases gradually (Figure S11f).

To further explore the electrochemical mechanism of CMPs during charging and discharging processes. The HOMO (highest occupied orbit)/LUMO (lowest unoccupied orbit) energy levels and orbital distributions of TBP-CMP and TB-CMP are then calculated using Density functional theory (DFT) (Figure 5a). Studies have demonstrated that the lower the LUMO energy level, the greater the ability to accept electrons and the greater the oxidation capacity. Conversely, the higher HOMO energy levels represent a lower ionization potential and better reducibility. Further, a narrower LUMO-HOMO gap (E_g) also indicates the greater electronic conductivity.^[47,48] Therefore, the performance of the electrode materials can be verified by quantitative comparison of LUMO, HOMO and E_g calculated by DFT for various electrode materials. Clearly, TBP-CMP have a smaller LUMO value, a higher HOMO value and a narrower band gap ($E_g = 2.33 \text{ eV}$). The result indicates that the TBP-CMP has higher electron conductivity, which facilitates the transfer of electrons along the polymer backbone during the charging and discharging processes. Therefore, TBP-CMP and TBP-CMP@CNT have higher electrochemical performance. Figure 5(b) shows the molecular electrostatic potential (MESP) of TBP-CMP and TB-CMP, where the blue area represents that the

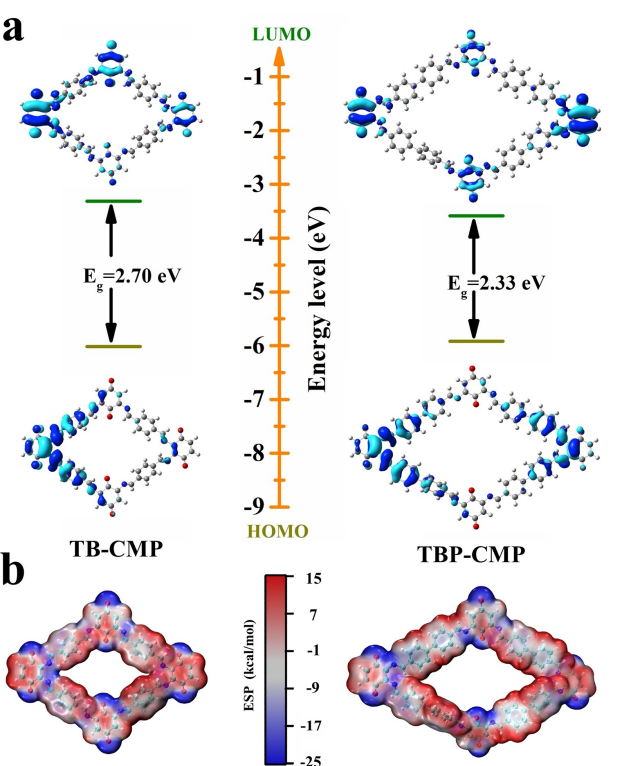


Figure 5. a) HOMO/LUMO energy level and orbits distribution of TB-CMP and TBP-CMP. b) MESP of TB-CMP and TBP-CMP.

electrostatic potential on the van der Waals surface is negative, and the red area represents that is positive.^[49,50] It can be seen that the oxygen and nitrogen atoms present more negative electrostatic potential values in the blue area, thus the functional groups containing oxygen and nitrogen atoms preferentially combine with lithium ions and then lithium ions bind to the unsaturated carbon atom in the benzene ring.

Subsequently, the storage mechanism is further confirmed by ex-situ FT-IR spectra of TBP-CMP@CNT electrode materials at different charge and discharge states (Figure 6a, b). Obviously,

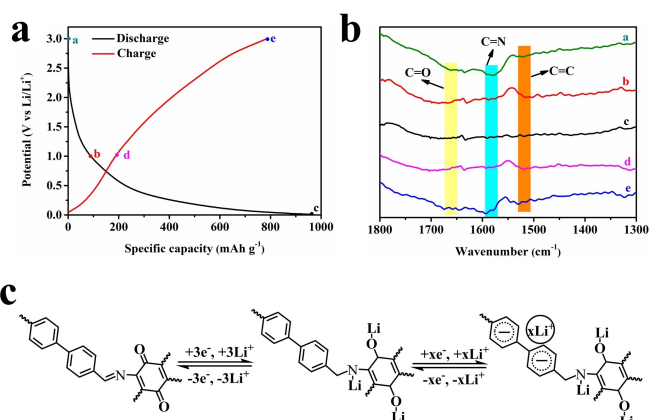


Figure 6. a) The galvanostatic charge-discharge curves of TBP-CMP@CNT, and b) the corresponding ex-situ FT-IR spectroscopy at different states of GCD as marked in (a). c) The possible lithium storage mechanism.

when the discharge reaches 0.01 V, the strong stretching vibration peak belonging to the C=O group near 1670 cm⁻¹ gradually weakens and disappears, representing the transformation of the C=O group to the Li—O—C group. When charge to 3 V, the characteristic peak of the C=O group gradually recovered, representing the desorption of lithium ions. Besides, the characteristic peaks corresponding to the C=N group (1605 cm⁻¹) and C=C group (1513 cm⁻¹) also show the same trend. The results of ex-situ FT-IR demonstrate that the C=O, C=N, and C=C groups all undergo lithium ions adsorption and desorption during the electrochemical reaction. Based on the theoretical calculation and experimental characterizations, the possible storage mechanism of Li⁺ is proposed in Figure 6(c), which contains multi-electron redox-reactions at C=O, C=N and benzene rings by the accommodation of Li⁺.

Conclusion

In this work, we prepared two carbonyl-rich imine-based CMPs integrated with CNTs (TBP-CMP@CNT and TB-CMP@CNT) by a one-step polymerization method, and used them as the anode-active materials for LIBs. Benefiting from the large π-conjugated structure, the abundant redox active centers and high active site utilization, TBP-CMP@CNT shows good electrochemical performance, including a high specific capacity of 954.6 mAh g⁻¹ at 0.05 A g⁻¹, a good reversible capacity of 521.2 mAh g⁻¹ after 1000 cycles at 1 A g⁻¹, and a good rate capacity of 221.5 mAh g⁻¹ even at 2 A g⁻¹. In addition, the redox activity of TBP-CMP@CNT based on multiple active sites has been confirmed by both experimental results and theoretical calculations. This work demonstrates that rationally designing CMPs with multiple active sites and more exposed active site utilization is viable for building next-generation environmentally friendly organic anode materials for sustainable energy storage devices.

Experimental Section

Synthesis of TB-CMP@CNT and TBP-CMP@CNT:

The in-situ growth of CMP on the surface of CNTs was prepared by a direct hydrothermal method.^[39] A 5 mL Pyrex tube was charged with 1 mL dioxane, 0.5 mL 6 M AcOH, and 20 mg CNT with sonication for 30 min, then charged with 12 mg (60 μmol) TABQ and 16 mg (120 μmol) BPDA (or BDA) with sonication for 30 min. Subsequently, the Pyrex tube was flame sealed after three degassing cycles and then heated at 150 °C for 3 days. After cooling to room temperature, the precipitate was collected by filtration and washed with EtOH, acetone, and DMF, respectively. Finally, the powder was dried under vacuum at 100 °C for 10 h. The same reaction without CNTs synthesized TB-CMP and TBP-CMP.

Acknowledgements

This work is financially supported by the National Natural Science Foundation of China (Grant No. 21965025) and Jilin Scientific and

Technological Development Programs (Grant No. 20200201240JC).

Conflict of Interest

The authors declare no conflict of interest.

Data Availability Statement

Research data are not shared.

Keywords: conjugated carbonyl groups • conjugated microporous polymers • imine groups • lithium-ion batteries • multi-active sites

- [1] M. Armand, J. M. Tarascon, *Nature* **2008**, *451*, 652–657.
- [2] X. Chi, M. Li, J. Di, P. Bai, L. Song, X. Wang, F. Li, S. Liang, J. Xu, J. Yu, *Nature* **2021**, *592*, 551–557.
- [3] L. Zhou, S. Jo, M. Park, L. Fang, K. Zhang, Y. Fan, Z. Hao, Y. M. Kang, *Adv. Energy Mater.* **2021**, *11*, 2003054.
- [4] A. Yoshino, *Angew. Chem. Int. Ed.* **2012**, *51*, 5798–5800; *Angew. Chem.* **2012**, *124*, 5898–5900.
- [5] X. Chen, X. Q. Zhang, H. R. Li, Q. Zhang, *Batteries & Supercaps* **2019**, *2*, 128–131.
- [6] H. G. Wang, H. Wang, Z. Si, Q. Li, Q. Wu, Q. Shao, L. Wu, Y. Liu, Y. Wang, S. Song, H. Zhang, *Angew. Chem. Int. Ed.* **2019**, *58*, 10204–10208; *Angew. Chem.* **2019**, *131*, 10310–10314.
- [7] J. Zhao, M. Zhou, J. Chen, L. Tao, Q. Zhang, Z. Li, S. Zhong, H. Fu, H. Wang, L. Wu, *Chem. Eng. J.* **2021**, *425*, 131630.
- [8] X. Cui, H. Dong, S. Chen, M. Wu, Y. Wang, *Batteries & Supercaps* **2021**, *4*, 72–97.
- [9] Q. Li, H. Wang, H. G. Wang, Z. Si, C. Li, J. Bai, *ChemSusChem* **2020**, *13*, 2449–2456.
- [10] C. Peng, G.-H. Ning, J. Su, G. Zhong, W. Tang, B. Tian, C. Su, D. Yu, L. Zu, J. Yang, M. F. Ng, Y. S. Hu, Y. Yang, M. Armand, K. P. Loh, *Nat. Energy* **2017**, *2*, 17074–17082.
- [11] G. Zhao, Y. Zhang, Z. Gao, H. Li, S. Liu, S. Cai, X. Yang, H. Guo, X. Sun, *ACS Energy Lett.* **2020**, *5*, 1022–1031.
- [12] A. Molina, N. Patil, E. Ventosa, M. Liras, J. Palma, R. Marcilla, *Adv. Funct. Mater.* **2020**, *30*, 1908074.
- [13] J. Bitenc, A. Scafuri, K. Pirnat, M. Lozinšek, I. Jerman, J. Grdadolnik, B. Fraisse, R. Berthelot, L. Stievano, R. Dominko, *Batteries & Supercaps* **2021**, *4*, 214–220.
- [14] K. Li, Y. Wang, B. Gao, X. Lv, Z. Si, H. G. Wang, *J. Colloid Interface Sci.* **2021**, *601*, 446–453.
- [15] C. Wu, M. Hu, X. Yan, G. Shan, J. Liu, J. Yang, *Energy Storage Mater.* **2021**, *36*, 347–354.
- [16] H. G. Wang, Y. Wang, Q. Wu, G. Zhu, *Mater. Today* **2022**, *52*, 269–298.
- [17] Z. Song, Y. Qian, M. L. Gordin, D. Tang, T. Xu, M. Otani, H. Zhan, H. Zhou, D. Wang, *Angew. Chem. Int. Ed.* **2015**, *54*, 13947–13951; *Angew. Chem.* **2015**, *127*, 14153–14157.
- [18] H. G. Wang, Q. Li, Q. Wu, Z. Si, X. Lv, X. Liang, H. Wang, L. Sun, W. Shi, S. Song, *Adv. Energy Mater.* **2021**, *11*, 2100381.
- [19] Y. An, S. Tan, Y. Liu, K. Zhu, L. Hu, Y. Rong, Q. An, *Energy Storage Mater.* **2021**, *41*, 354–379.
- [20] J. Yu, X. Chen, H. G. Wang, B. Gao, D. Han, Z. Si, *Sci. China Mater.* **2022**, *65*, 2354–2362.
- [21] H. Wang, Q. Wu, Y. Wang, X. Lv, H. G. Wang, *J. Colloid Interface Sci.* **2022**, *606*, 1024–1030.
- [22] J. M. Lee, A. I. Cooper, *Chem. Rev.* **2020**, *120*, 2171–2214.
- [23] Y. Xu, S. Jin, H. Xu, A. Nagai, D. Jiang, *Chem. Informationsdienst* **2013**, *44*, 8012–8031.
- [24] N. Chaoui, M. Trunk, R. Dawson, J. Schmidt, A. Thomas, *Chem. Soc. Rev.* **2017**, *46*, 3302.
- [25] A. I. Cooper, *Adv. Mater.* **2009**, *21*, 1291–1295.

- [26] L. W. Luo, C. Zhang, P. Xiong, Y. Zhao, W. Ma, Y. Chen, J. H. Zeng, Y. Xu, J. X. Jiang, *Sci. China Chem.* **2021**, *64*, 72–81.
- [27] K. Li, Q. Li, Y. Wang, H. G. Wang, Y. Li, Z. Si, *Mater. Chem. Front.* **2020**, *4*, 2697–2703.
- [28] A. Molina, N. Patil, E. Ventosa, M. Liras, J. Palma, R. Marcilla, *Adv. Funct. Mater.* **2019**, *30*, 1908074.
- [29] Z. Ouyang, D. Tranca, Y. Zhao, Z. Chen, X. Fu, J. Zhu, G. Zhai, C. Ke, E. Kymakis, X. Zhuang, *ACS Appl. Mater. Interfaces* **2021**, *13*, 9064–9073.
- [30] Z. Chen, W. Li, Y. Dai, N. Xu, C. Su, J. Liu, C. Zhang, *Electrochim. Acta* **2018**, *286*, 187–194.
- [31] S. Zhang, W. Huang, P. Hu, C. Huang, C. Shang, C. Zhang, R. Yang, G. Cui, *J. Mater. Chem. A* **2015**, *3*, 1896–1901.
- [32] L. Bai, Q. Gao, Y. Zhao, *J. Mater. Chem. A* **2016**, *4*, 14106–14110.
- [33] D. H. Yang, Z. Q. Yao, D. Wu, Y. H. Zhang, Z. Zhou, X. H. Bu, *J. Mater. Chem. A* **2016**, *4*, 18621–18627.
- [34] Q. Xu, S. Tao, Q. Jiang, D. Jiang, *J. Am. Chem. Soc.* **2018**, *140*, 7429–7432.
- [35] L. Shu, J. Yu, Y. Cui, Y. Ma, Y. Li, B. Gao, H. G. Wang, *Int. J. Hydrogen Energy* **2022**, *47*, 10902–10910.
- [36] R. Shi, L. Liu, Y. Lu, Y. Li, S. Zheng, Z. Yan, K. Zhang, J. Chen, *Adv. Energy Mater.* **2021**, *11*, 2002917.
- [37] X. Chen, H. Zhang, C. Ci, W. Sun, Y. Wang, *ACS Nano* **2019**, *13*, 3600–3607.
- [38] H. Gao, Q. Zhu, A. R. Neale, M. Bahri, X. Wang, H. Yang, L. Liu, R. Clowes, N. D. Browning, R. S. Sprick, M. A. Little, L. J. Hardwick, A. I. Cooper, *Adv. Energy Mater.* **2021**, *11*, 2101880.
- [39] K. C. Ranjeesh, R. Illathvalappil, S. D. Veer, J. Peter, V. C. Wakchaure, Goudappagouda, K. V. Raj, S. Kurungot, S. S. Babu, *J. Am. Chem. Soc.* **2019**, *141*, 14950–14954.
- [40] O. Buyukcakir, J. Ryu, S. H. Joo, J. Kang, R. Yuksel, J. Lee, Y. Jiang, S. Choi, S. H. Lee, S. K. Kwak, S. Park, R. S. Ruoff, *Adv. Funct. Mater.* **2020**, *30*, 2003761.
- [41] X. Yang, C. Lin, D. Han, G. Li, C. Huang, J. Liu, X. Wu, L. Zhai, L. Mi, *J. Mater. Chem. A* **2022**, *10*, 3989–3995.
- [42] T. Li, L. Wang, J. Li, *Electrochim. Acta* **2022**, *408*, 139947.
- [43] Z. Lei, Q. Yang, Y. Xu, S. Guo, W. Sun, H. Liu, L. P. Lv, Y. Zhang, Y. Wang, *Nat. Commun.* **2018**, *9*, 576.
- [44] S. Zheng, L. Miao, T. Sun, L. Li, J. Chen, *J. Mater. Chem. A* **2021**, *9*, 2700–2705.
- [45] H. Kang, H. Liu, C. Li, L. Sun, C. Zhang, H. Gao, J. Yin, B. Yang, Y. You, K. C. Jiang, H. Long, S. Xin, *ACS Appl. Mater. Interfaces* **2018**, *10*, 37023–37030.
- [46] Q. Wu, Q. Shao, Q. Li, Q. Duan, Y. Li, H. G. Wang, *ACS Appl. Mater. Interfaces* **2018**, *10*, 15642–15651.
- [47] Q. Zhao, Y. Lu, J. Chen, *Adv. Energy Mater.* **2017**, *7*, 1601792.
- [48] Y. Kim, J. Hong, J. H. Oh, C. Yang, *Chem. Mater.* **2013**, *25*, 3251–3259.
- [49] Y. Lu, X. Hou, L. Miao, L. Li, R. Shi, L. Liu, J. Chen, *Angew. Chem. Int. Ed.* **2019**, *58*, 7020–7024; *Angew. Chem.* **2019**, *131*, 7094–7098.
- [50] H. G. Wang, H. Wang, Y. Li, Y. Wang, Z. Si, *J. Energy Chem.* **2021**, *58*, 9–16.

Manuscript received: September 27, 2022

Revised manuscript received: October 25, 2022

Accepted manuscript online: November 2, 2022

Version of record online: November 18, 2022